NeuroImage 202 (2019) 116074

Contents lists available at ScienceDirect

NeuroImage

journal homepage: www.elsevier.com/locate/neuroimage

Computing distance information from landmarks and self-motion cues - Differential contributions of anterior-lateral vs. posterior-medial entorhinal cortex in humans

Xiaoli Chen [a,*], Paula Vieweg [b], Thomas Wolbers [a,c,d]

[a] Aging & Cognition Research Group, German Center for Neurodegenerative Diseases (DZNE), Magdeburg, Germany
[b] Institute of Psychology, University of Leipzig, Leipzig, Germany
[c] Center for Behavioural Brain Sciences (CBBS), Otto-von-Guericke University, Magdeburg, Germany
[d] Medical Faculty, University Hospital Magdeburg, Otto-von-Guericke-University, Magdeburg, Germany

ARTICLE INFO

Keywords:
Spatial cognition
Navigation
Landmark
Path integration
Entorhinal cortex
Ultra-high field fMRI

ABSTRACT

Landmarks and path integration cues are two important sources of spatial information for navigation. For example, both can be used to compute positional information, which, in rodents, has been related to computations in the entorhinal cortex. In humans, however, if and how the entorhinal cortex supports landmark-based navigation and path integration is poorly understood. To address this important question, we developed a novel spatial navigation task in which participants learned a target location and judged relative positions of test locations in relation to the target. Landmarks and path integration cues were dissociated, and their reliability levels were manipulated. Using fMRI adaptation, we investigated whether spatial distances among the test locations were encoded in the BOLD responses, separately for landmarks and self-motion cues. The results showed that the anterior-lateral entorhinal cortex adapted to the distance between successively visited test locations when landmarks were used for localization, meaning that its activation decreased as the distance between the currently occupied location and the preceding location decreased. In contrast, the posterior-medial entorhinal cortex adapted to between-location distance when path integration cues were used for localization. In addition, along with the hippocampus and the precuneus, both entorhinal subregions showed stronger activation in correct trials than incorrect trials, regardless of cue type and reliability level. Together, these findings suggest that subdivisions of entorhinal cortex encode fine-grained spatial information for different spatial cues, which provides important insights into how the entorhinal cortex supports different modes of spatial navigation.

1. Introduction

Spatial navigation is an indispensable skill for the survival of humans and non-human animals. Spatial navigation can rely on self-motion cues, e.g., proprioceptive cues, vestibular cues, and optic flow. With self-motion cues, one needs to continuously integrate movement inputs over time and distance to infer self-location in the environment, a process referred to as path integration (Etienne and Jeffery, 2004; Mittelstaedt and Mittelstaedt, 1980). Spatial navigation can also rely on static environmental cues such as landmarks, which are directly informative of one's location. Both landmarks and self-motion cues can be useful for providing fine-grained spatial information to support precise spatial navigation, such as computing spatial distances among different locations. The representation of fine-grained spatial information is also necessary for building a 'cognitive map', a flexible mental representation of the environment that contains spatial information between locations (Tolman, 1948).

Spatial navigation is a complex phenomenon, due to the fact that landmark-based navigation and path integration are relatively independent cognitive processes, yet dynamically interact with each other during navigation (Etienne et al., 1996). First, as to their relative independence, there is little competition between landmarks and path integration cues. For example, varying the cue quality of landmarks (e.g., stability and richness) does not affect path integration performance in humans, meaning that landmark-based navigation does not overshadow path integration (Chen et al., 2017). Similarly, in rodents, navigating with a beacon landmark does not overshadow the ability to go back home with path integration cues alone after food retrieval; and conversely, path

* Corresponding author. German Centre for Neurodegenerative Diseases (DZNE), Leipziger Str. 44, Haus 64, 39120, Magdeburg, Germany.
E-mail address: chenxiaoli54@gmail.com (X. Chen).

https://doi.org/10.1016/j.neuroimage.2019.116074
Received 17 March 2019; Received in revised form 5 July 2019; Accepted 2 August 2019
Available online 3 August 2019

integration experience does not block the homing ability with the beacon landmark (Shettleworth and Sutton, 2005). In addition, in humans, landmark-based navigation performance and path integration performance are overall weakly or moderately correlated across participants (Chen et al., 2017). These findings together suggest a mutual independence of landmark-based navigation and path integration, which is in contrast to the strong competition usually observed between different types of environmental cues (e.g., Cheng, 1986; Diez-Chamizo et al., 1985; Wilson and Alexander, 2008). Second, as to dynamic interactions, behavioral studies have shown (i) that landmarks can be used to correct the accumulated noise in path integration (Kelly et al., 2008) or reset the path integrator (Etienne et al., 2004; Zhao and Warren, 2015), (ii) that path integration can be used to distinguish ambiguous (Etienne et al., 1998) or unreliable landmarks (Zhao and Warren, 2015), and (iii) that landmarks and self-motion cues can be combined to improve navigation performance (Bates and Wolbers, 2014; Chen et al., 2017; Nardini et al., 2008; Zhao and Warren, 2015). Therefore, to understand the complexity of spatial navigation at the neuronal level, it is critical to first understand how the brain supports path integration vs. landmark-based positional coding.

At the neuronal level, entorhinal cortex (EC) is a central component of the navigation circuit as it computes positional information from incoming sensory cues (Moser et al., 2008). Despite some evidence against the role of EC in path integration (e.g., Shrager et al., 2008), many studies have linked EC to fine-grained spatial computations in both path integration and landmark-based navigation. Various types of spatially modulated neurons have been recorded in EC in relation to landmarks and/or self-motion cues. First, entorhinal grid cells are influenced by both self-motion cues and landmark cues (Hafting et al., 2005), and grid cell firing is related to path integration in both rodents (Gil et al., 2018) and humans (Stangl et al., 2018). Grid cells could provide an intrinsic metric necessary for path integration (McNaughton et al., 2006; Moser and Moser, 2008) and support the computations of fine-grained spatial information, e.g. travelled distance, during path integration. Second, several studies have recorded neurons in the rodent EC whose firing is spatially modulated by local landmarks, because they display orientation-tuning and/or distance-tuning to local landmarks (Deshmukh and Knierim, 2011; Wang et al., 2018). This could provide a neuronal mechanism of extracting fine-grained spatial information from landmarks, e.g., self-distance to the landmark. Accordingly, in rodents, lesions to EC impair both path integration (Jacob et al., 2017; Parron and Save, 2004) and landmark-based navigation (Parron et al., 2004). Together, these findings suggest that EC contributes to both landmark-based navigation and path integration by computing fine-grained spatial information from both landmarks and self-motion cues.

In line with the behavioural evidence suggesting differential neuronal mechanisms for landmark-based navigation and path integration, rodent studies have observed differences between the lateral EC (LEC) and medial EC (MEC). Indeed, one view posits that the segregation is content-based and that the rodent LEC and MEC process local landmark information and self-motion information, respectively (Knierim et al., 2014). In support of this view, recent studies have demonstrated a critical role of grid cells and MEC in path integration (Chen et al., 2015; Gil et al., 2018; Jacob et al., 2017; Stangl et al., 2018), resonating with the theoretical considerations linking grid cells and MEC to path integration (McNaughton et al., 2006; Moser and Moser, 2008). In addition, rodent studies have reported neurons in LEC whose firing behavior is modulated by the spatial relation to local objects (Deshmukh and Knierim, 2011; Wang et al., 2018), and LEC lesions impair spatial learning with local landmarks (Kuruvilla and Ainge, 2017). These studies also argue against the conventional hypothesis of a rigid dictochomy of nonspatial vs. spatial processing between LEC and MEC (Witter, 1993; Witter et al., 2017). Parallel to these findings in rodents, human fMRI studies have also shown a functional segregation in the human EC between its anterior-lateral subregion (alEC) and its posterior-medial subregion (pmEC), and the human alEC and pmEC are considered as functional homologs to the rodent LEC and MEC, respectively (Maass et al., 2015; Schröder et al., 2015). Based on these findings, we sought to investigate neural mechanisms of landmark-based navigation and path integration in alEC and pmEC.

Understanding the spatial computations carried out in subregions of EC is crucial for developing a full understanding of how the human brain supports navigational behavior. While previous studies have examined the neural basis of pure path integration with no landmark cues provided (Chrastil et al., 2015; Gil et al., 2018; Jacob et al., 2017; Stangl et al., 2018; Wolbers et al., 2007) or pure landmark-based navigation with self-motion cues discarded by disorientation manipulations (Sutton et al., 2010), landmark-based navigation and path integration have never been directly compared in the same spatial context in neuroscience studies. As a consequence, it remains unclear whether the reported mechanisms are unique to the examined navigation process or generalizable to the other unexamined process. In addition, human neuroimaging studies of this kind did not examine EC or EC subregions for various reasons (e.g., excessive signal dropout (Chrastil et al., 2015)).

To address the important question of how landmark-based navigation and path integration are processed in the human EC, we designed a novel navigation task, in which landmarks and self-motion cues were dissociated and contrasted in the same spatial context. This approach allowed for a direct comparison between the two navigation processes, which is critical for revealing process-specific neural mechanisms as well as for controlling confounds like attentional engagement, task demand, and individual idiosyncrasy. Specifically, participants were required to judge relative positions of test locations in relation to a target location, with either landmark cues alone or self-motion cues alone. The test locations and the target location were arranged on a linear track, so only distance estimation was required to complete the task. Using ultra-high field magnetic resonance imaging (MRI) at 7 T and a repetition suppression approach, we investigated distance coding for landmarks and self-motion cues separately, i.e., whether spatial distances among the test locations were encoded in the BOLD responses. Our analysis focused on the right EC (see the rationale of our choice of region of interest (ROI) in section 2.5). Together, this approach enabled us to test how different entorhinal subregions in humans support the fine-grained computations of distance information in distinct modes of spatial navigation.

2. Material and methods

2.1. Participants

Twenty-four young healthy adults participated in the study (15 males). They were right-handed, had normal or corrected-to-normal vision, and had no history of neurological diseases. Two participants were excluded from further analysis because of low-quality T2-weighted structural scans caused by excessive head motion. This resulted in 22 participants in total in the data analysis (13 males; age range = 22 to 37, mean (SD) age = 27.9 (4.2)). All participants gave written informed consent and received monetary compensation. The study was approved by the local ethics committee of Otto-von-Guericke University, Magdeburg, Germany.

2.2. Materials

All the tasks were performed in a virtual reality environment (Fig. 1). Graphics were rendered using Vizard software (WorldViz, version 5, Santa Barbara, CA). In the familiarization stage prior to MRI scanning, participants performed some tasks in the virtual environment on an Alienware laptop. During MRI scanning, the virtual environment was projected onto a screen mounted at the end of the MRI bed and reflected via an IR-reflecting first surface mirror. The display size (22.9 cm × 12.9 cm) and the eye-to-screen distance (100 cm) were matched in the familiarization stage and the MRI scanning stage.

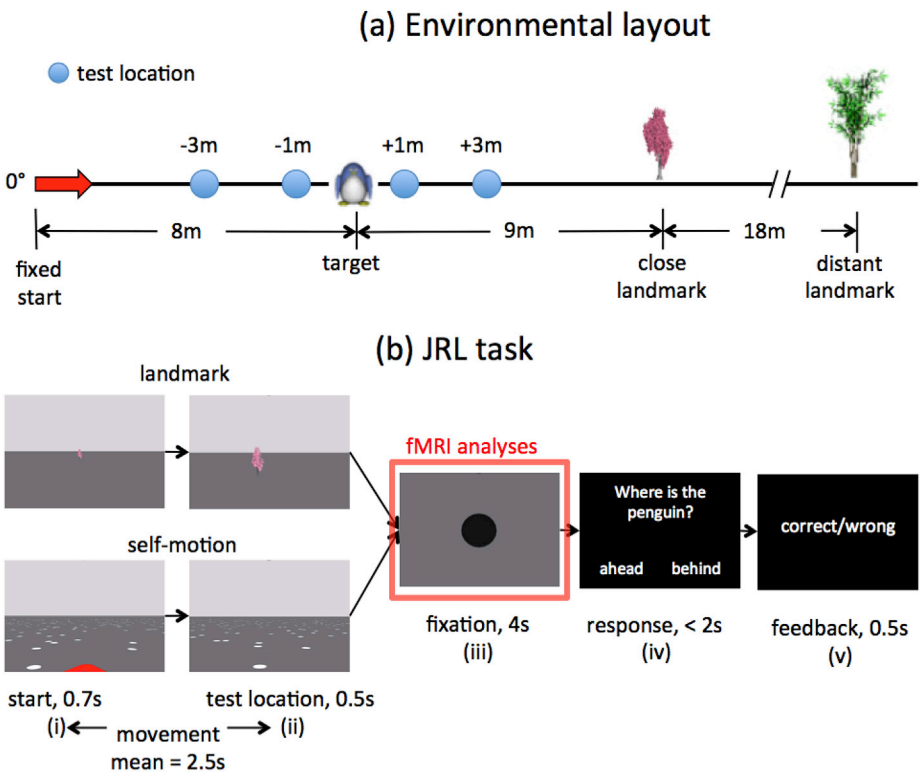

Fig. 1. Experimental setup. (a), schematic of the environmental layout. The target (penguin) was 8 m away from the red arrow, which pointed to the target along 0° perspective. The four blue dots represent the four test locations – 3 m behind (-3 m), 1 m behind (-1 m), 1 m ahead of (+1 m), and 3 m ahead of (+3 m) the target, respectively. The four test locations lied on an imaginary linear track from the red arrow to the target. The red arrow was the fixed starting position for the movement in the self-motion conditions. The close landmark (the cherry tree) was 9 m from the target, and the distant landmark (the green tree) was 27 m from the target. For illustrative purposes, the distant landmark is placed closer to the target than it really was. (b), time course of the judgment of relative location (JRL) task in the landmark conditions (upper, the close landmark is displayed) and the self-motion conditions (lower): phase (i), the participant stands at the starting position, which was randomized from trial to trial around the red arrow in the landmark conditions and fixed at the red arrow in the self-motion conditions; phase (ii), the participant is passively transported to the test location; phase (iii), at the test location, the subject's viewpoint smoothly turns down and then faces vertically downward at the ground for 4 s; phase (iv), the participant judges the relative location of the penguin; phase (v), feedback is provided. Note that the red arrow was invisible in the landmark conditions and visible in the self-motion conditions. Phase (iii), highlighted in a red box, was the event of interest to estimate distance coding from the fMRI data.

Fig. 1a shows the schematic of the environmental setup. Participants learned the location of a target (i.e. the penguin), which was fixed in the environment, and were tested on their memory. Two different landmarks were used, with one positioned closer to the target than the other (the two trees in Fig. 1a; counterbalanced across participants). The distance from the close landmark to the penguin was 9 m, and the distance from the distant landmark to the penguin was 27 m. The close landmark was 1.5 m tall, and the distant landmark was 4.5 m tall. When standing at the penguin's location, the vertical and horizontal visual angles subtended by the close landmark and the distant landmark were matched. Four different test locations were evenly spaced around the penguin's location along the 0° perspective (Fig. 1a, blue dots). Two test locations were 1 m (-1 m) and 3 m (-3 m) behind the penguin. The other two were 1 m (+1 m) and 3 m (+3 m) in front of the penguin. There was a red arrow, whose location was fixed in the environment. The distance from the penguin to the red arrow was 8 m. The red arrow, the target, and the four test locations all lied in an imaginary straight line. The two landmarks lied almost on this imaginary straight line, but with a small offset of 0.5 m to the left and right from the 0° perspective, respectively. In trials where only self-motion cues were available, there was a collection of limited lifetime white dots on the ground to provide optic flow information during self-movement (Fig. 1b, lower). In order to enhance the sense of spatial immersion, this layout was situated in a rich background environment surrounded by mountains and trees. The background environment was visible occasionally (Figure A1, Appendix A).

2.3. Task

Participants completed the judgment of relative location task (JRL task), in which the participant was passively transported to one of the four test locations (Fig. 1a, blue dots) around the target location and judged the relative position of the target location to the occupied test location. The passive movement was restricted to be linear, and the movement speed was randomly sampled from a uniform distribution [2 m/s, 5 m/s] on a trial-by-trial basis to avoid pure timing or counting strategies. The duration of the passive movement varied from trial to trial and lasted about 2.5 s on average (i.e., from (i) to (ii) in Fig. 1b). The passive movement always started from the 0° perspective, aligned with the pointing direction of the red arrow (Fig. 1a). After they arrived at the test location (Fig. 1b, (ii)), the camera smoothly turned down by 90° and faced vertically downward at a large black dot on the blank ground for 4 s (Fig. 1b, (iii)). After the 4 s, participants judged whether the penguin's location was ahead of or behind them within 2 s (Fig. 1b, (iv)). Finally, feedback was provided, telling participants whether their responses were correct or incorrect (Fig. 1b, (v)). The penguin remained invisible throughout the trial. The background environment remained invisible (Figure A1, Appendix A).

Landmarks and self-motion cues were dissociated and manipulated in reliability in the JRL task. This resulted in four different conditions - landmark high, landmark low, self-motion high, and self-motion low. The dissociation of landmarks and self-motion cues followed the same logic in the established behavioral paradigm used to investigate combination of these two cue types in the 2-dimensional space (Bates and Wolbers, 2014; Chen et al., 2017; Nardini et al., 2008; Zhao and Warren, 2015). In the two landmark conditions (Fig. 1b, upper), the starting position of the passive movement was variable on a trial-by-trial basis. The starting position in each trial was randomly sampled from a uniform distribution [-4.5 m, 4.5 m] around the position of the red arrow (Fig. 1a). In this way, in a given trial, participants would not know the distance they needed to travel to the target and thus could not perform path integration to solve the task. This random placement of the participant's initial position along the linear track is analogous to the 'disorientation manipulation' used to eliminate self-motion information in other established navigation tasks (Cheng, 1986; Sutton et al., 2010). The movement was aligned with the

pointing direction of the red arrow. The red arrow was invisible throughout the trial. In addition, the ground remained blank, providing no optic flow information for path integration. Therefore, participants were forced to rely on the landmark only. Only the close landmark was displayed in the landmark high condition, and only the distant landmark was displayed in the landmark low condition.

The two self-motion conditions provided only self-motion cues for localization (Fig. 1b, lower), and no landmarks were displayed. The passive movement always started from the fixed red arrow in each trial, so participants knew how far they needed to travel to reach the target and could hence perform path integration to complete the task. The movement direction was aligned with the pointing direction of the red arrow, which was visible (Fig. 1a). White limited lifetime dots (life time = 1 s) were displayed on the ground, providing optic flow information for path integration. The dots were moving along or against the movement direction of the participant. The speed of each dot was randomly sampled from a normal distribution with a mean of 0 m/s and a standard deviation of 0.2 m/s in the self-motion high condition. In the self-motion low condition, the normal distribution had a mean of 0 m/s and a standard deviation of 6 m/s. Therefore, the white dots moved considerably more violently in the self-motion low condition than in the self-motion high condition. There were approximately 1000 dots appearing on the ground at a given time. The dot area was linked to the participant's self-location. If we define the instantaneous location of the participant as the origin and 0° perspective as the y-axis, these dots were evenly distributed in a rectangular area [-35 m, 35 m] horizontally and [-10 m, 60 m] in depth. Estimating travelled distances is considered a form of path integration, since self-motion inputs need to be continuously integrated during the linear movement (Chrastil et al., 2017; Jacob et al., 2017; Marlinsky, 1999; Philbeck et al., 2004).

A compound condition was also included, in which both landmark and self-motion cues were available for self-localization. In each trial, it was randomly determined whether the two cues were high or low in reliability. However, cue combination was not our primary interest here and it only consisted of a limited number of trials. The purpose of including some compound trials in the current study was to collect pilot data to guide future experiments on cue combination. Therefore, the results of the compound condition are not reported here.

The procedure also contained a limited number of learning trials, in which the participant learned the target location and refreshed their memory of the target location in the middle of testing. Detailed description of learning trials can be found in the supplementary materials (Appendix A, section 2). Learning trials were not the focus of the study and hence not analyzed.

2.4. Procedure

Chronologically, the procedure consisted of a familiarization stage, a practice stage during structural MRI scanning, and a test stage during functional MRI scanning. The familiarization stage was conducted outside of the scanner, when participants were familiarized with the virtual environment and joystick operation. The practice and test stages were conducted inside the scanner, when participants performed the JRL task. The test stage represented the main part of the experiment and was the focus of our data analysis.

In the familiarization stage, participants were required to navigate around with the background environment visible (Figure A1, Appendix A). Five balls of different colors were scattered in the environment. Participants needed to navigate to collect the balls and remember their colors. Participants also performed a perspective-taking task intermittently: while standing at the position of the red arrow and facing the direction the arrow pointed to, participants judged whether an object (one of the five balls, some objects in the background environment) was to their left side or right side. Sometimes, participants needed to take the perspectives of the −30° and 30° vantage points (Figure A2a, Appendix A). This stage also served to increase the sense of spatial immersion throughout the experiment, since in the subsequent practice and test stages, participants performed the JRL task in the same but visually deprived environment with the background environment invisible (Fig. 1b).

After the familiarization stage, participants completed the practice stage while undergoing structural MRI scanning. No learning criterion was imposed, and there were a fixed number of trials for every participant. The practice stage consisted of two runs, and each run had five blocks. Each of the five blocks corresponded to one of the five conditions: landmark high, landmark low, self-motion high, self-motion low, and compound. In each block, participants performed four JRL trials, preceded by four learning trials. The five blocks were randomized in order within each run. The background environment remained invisible, but participants were required to perform the perspective-taking task prior to each block.

After the practice stage, participants completed the test stage while undergoing functional MRI scanning. The test stage consisted of two runs. Each run had five blocks, corresponding to the five conditions. The first block was always the compound condition, which contained four JRL trials, preceded by four learning trials. For the JRL trials, test locations were randomly selected and ordered in the compound condition. The four remaining blocks corresponded to the four conditions respectively - landmark high, landmark low, self-motion high, self-motion low - randomized in order. Each of the four blocks contained 20 JRL trials (five trials for each test location), preceded by four learning trials. For the JRL trials, we adopted a continuous carry-over design (Aguirre, 2007), with five types of events in the sequence – fixation periods at the four test locations (−3 m, −1 m, +1 m, and +3 m; Fig. 1b, (iii)), in which participants stayed at the test locations for 4 s, and null event, in which participants fixated their eyes at a cross displayed in the middle of the blank screen. Using the path-guided cycle, we generated de Bruijn sequences with 2nd order counterbalancing (Aguirre et al., 2011). This led to 25 events in total in a sequence, with five repetitions for each event type. We selected eight sequences with high detection power (>0.9) and low correlation coefficient ($|rs| < 0.13$), which were then randomly assigned to the four conditions in the two runs (Appendix A, section 3, Table A1). To allow the hemodynamic response to reach a steady state before the sequence started, we duplicated the very last event in the sequence and placed it at the very beginning. As in the practice stage, the background environment remained invisible, but participants were required to perform the perspective-taking task prior to each block.

2.5. MRI data acquisition, preprocessing, and anatomical masks

Structural and functional images were acquired in a 7T MR scanner (Siemens, Erlangen, Germany) at the Leibniz Institute for Neurobiology in Magdeburg with a 32-channel head coil (Nova Medical, Wilmington, MA). A high-resolution whole-brain T1-weighted structural scan was acquired with the following MP-RAGE sequence: TR = 1700 ms; TE = 2.01 ms; flip angle = 5°; slices = 176; orientation = sagittal; resolution = 1 mm isotropic. A partial-volume turbo spin echo high-resolution T2-weighted structural scan was acquired perpendicular to the long axis of the hippocampus (TR = 8000 ms; TE = 76 ms; flip angle = 60°; slices = 55; slice thickness = 1 mm; distance factor = 10%; in-plane resolution = 0.4 × 0.4 mm; echo spacing = 15.1 ms, turbo factor = 9, echo trains per slice = 57). Functional scans were acquired with a T2*-weighted 2D echo planar image slab centered on the hippocampus and parallel to its long axis (TR = 2000 ms, TE = 22 ms; flip angle = 85°; slices = 35; resolution = 1 mm isotropic, parallel imaging with grappa factor 1, echo spacing = 0.82 ms). We also obtained 10 vol of whole brain functional scans for the purpose of co-registering anatomical masks to functional scans (MP-RAGE sequence: TR = 5000 ms, TE = 22 ms; flip angle = 85°; slices = 100; resolution = 1.6 mm isotropic). The T1-weighted structural image was bias-corrected in SPM8. EPIs were motion and distortion corrected online via point spread function mapping (In and Speck, 2012). The functional scans were spatially smoothed with a 3 mm full-width

Table 1
ROI analysis of distance-based adaptation across experimental conditions. Results without the statistical outlier are listed in parentheses. Significant effects are highlighted in bold.

ROI	Condition	t	$p_{uncorrected}$	$p_{corrected}$	Cohen's d	BF
alEC	**Landmark high**	**2.722 (3.830)**	**0.007 (< 0.001)**	**0.035 (0.005)**	**0.580 (0.836)**	**0.124 (0.014)**
	Landmark low	−0.504 (0.625)	0.637 (0.267)	>0.999 (0.919)	−0.107 (0.136)	6.285 (2.559)
	Self-motion high	1.441 (1.362)	0.086 (0.095)	0.499 (0.542)	0.307 (0.297)	1.001 (1.096)
	self-motion low	0.628 (0.674)	0.272 (0.257)	0.924 (0.903)	0.134 (0.147)	2.601 (2.436)
pmEC	Landmark high	0.783 (1.567)	0.213 (0.066)	0.873 (0.420)	0.167 (0.342)	2.217 (0.830)
	Landmark low	0.060 (0.885)	0.476 (0.193)	0.993 (0.816)	0.013 (0.193)	4.286 (1.950)
	Self-motion high	0.854 (0.607)	0.196 (0.276)	0.844 (0.923)	0.182 (0.132)	2.055 (2.604)
	Self-motion low	0.204 (0.281)	0.428 (0.391)	0.988 (0.981)	0.043 (0.061)	3.819 (3.512)

half-maximum (FWHM) Gaussian filter. Fig. 2a shows the T2-weighted structural scan and a functional scan overlaid on the T1-weighted structural scan of a participant.

A plethora of neuroimaging and lesion studies in humans have shown a predominant involvement of the right medial temporal lobe in spatial navigation (Abrahams et al., 1997; Doeller et al., 2008; Philbeck et al., 2004; Wolbers et al., 2007). This hemispheric asymmetry has also been observed in human neuroimaging studies on spatial coding in EC during navigation (Doeller et al., 2010; Howard et al., 2014; Kunz et al., 2015). In rodents, although spatial neurons in MEC have been recorded in both hemispheres (e.g., Hafting et al., 2005), spatial neurons in LEC have only been described in the right hemisphere (Deshmukh and Knierim, 2011; Wang et al., 2018). Therefore, our analysis focused on the right EC as the ROI. However, for completeness, the results of the left EC are reported in the supplementary materials (Appendix A, section 9).

To obtain the anatomical masks for alEC and pmEC, we first manually segmented the right EC on coronal slices on the T2-weighted structural scan in ITK-SNAP (Version 3.4; www.itksnap.org; Yushkevich et al., 2006), following the protocol developed by Berron, Vieweg and colleagues (Berron et al., 2017). The manual segmentation was done by author XC, and then checked and adjusted by author PV. Next, the border between alEC and pmEC was determined as follows. The anatomical templates of alEC and pmEC from Maass et al. (2015) were first warped onto individual T1-weighted structural scans of our participants, using the nonlinear brain registration algorithms in Advanced Normalization Tools (ANTs) (i.e., the command "antsRegistrationSyNQuick.sh"). The warped templates were then co-registered to the T2-weighted structural scan in SPM12. The alEC-pmEC border in the warped anatomical templates was then copied to our manually segmented anatomical mask of the right EC on coronal slices on the T2-weighted structural scan in ITK-SNAP. We determined the alEC-pmEC border in this way for two reasons. First, we could not use the warped masks directly, because the anatomical mask for EC in Maass et al. (2015) used very different anatomical boundaries from the protocol we used for our manual segmentation (Berron et al., 2017). The protocol we used represents a coherent integration of existing anatomical findings, and therefore, the entorhinal boundaries were much more rigorously defined (Berron et al., 2017). Second, we could not apply the verbal description of manual demarcation of alEC and pmEC in Maass et al. (2015) directly to our manual segmentation on the T2-weighted structural scan. Our T2-weighted structural scan was acquired at an orientation perpendicular to the long axis of the hippocampus, which was different from the T1-weighted structural scan in Maass et al. (2015). Following their verbal description on the T2-weighted structural scan would result in an alEC-pmEC border positioned more posteriorly from its correct location. Fig. 2b depicts the anatomical masks of the right alEC and pmEC in the 3D brain extracted from the T1-weighted structural scan of a typical participant, with the right hippocampus also rendered for reference.

Finally, the anatomical masks were co-registered to the mean functional scan of the first run in SPM12, using the following procedure: first, the mean whole-volume functional scan was co-registered to the mean functional scan; second, the T2-weighted structural scan, along with the anatomical masks, were co-registered to the mean whole-volume functional scan obtained from the first step; third, the co-registered T2-weighted structural scan and anatomical masks were re-sliced using nearest neighbours interpolation, with the mean functional scan as the reference image.

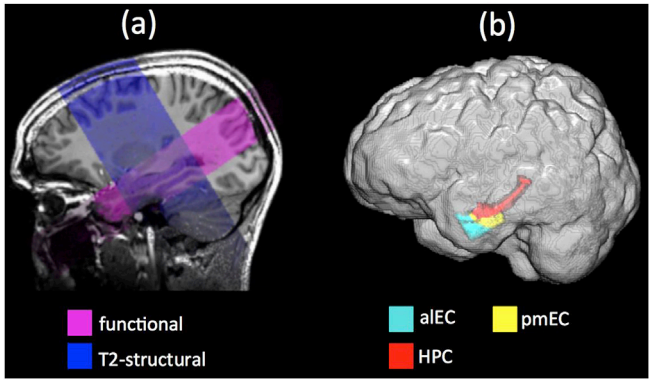

Fig. 2. MRI scans and manual segmentation. (a), for a typical participant, from the sagittal view, the T2-weighted structural scan (blue) and the functional scan (pink) are overlaid on the T1-weighted structural scan. (b), for a typical participant, anatomical masks of the anterior-lateral entorhinal cortex (alEC, cyan) and the posterior-medial entorhinal cortex (pmEC, yellow) in the right hemisphere are rendered in the participant's 3D brain extracted from the T1-weighted structural scan (seen from the left hemisphere). The right hippocampus (HPC, red) is also rendered for reference.

2.6. Behavioral analysis

Given that the JRL trials in the test stage were the primary focus of the study, we calculated behavioral accuracy based on whether the answer was correct (coded as 1) or not (coded as 0), with a chance level of 0.5. The analysis included trials from the two test runs. Repeated measures analysis of variance (ANOVA) was conducted first, with cue type and cue reliability as independent factors, followed by paired t-tests if necessary. In addition to the inferential tests, we also computed objective Bayes factors (BFs), which express the likelihood ratio of the null hypothesis over the alternative (Rouder et al., 2009). We used r scale of 0.707. A Bayes factor smaller than 1 means stronger evidence supporting the alternative, whereas a Bayes factor greater than 1 means stronger evidence supporting the null. For interpretation (i.e., Jeffreys's benchmarks; Jeffreys, 1961), a Bayes factor smaller than 1/3 means substantial evidence for the alternative hypothesis, whereas a Bayes factor larger than 3 indicates substantial evidence for the null hypothesis. A Bayes factor smaller than 0.1 (or larger than 10) indicates strong evidence for the alternative (or the null). A Bayes factor between 1/3 and 1 (or between 1

and 3) indicates anecdotal evidence for the alternative (or the null).

2.7. fMRI analysis

Statistical analyses of the fMRI data were based on general linear models (GLM) as implemented in SPM12. We constructed three GLMs to address two research questions: first, whether there was neural coding of distances among test locations; second, how the brain's functional activation was affected by the experimental manipulations of cue type and cue reliability, and successful navigation. To reiterate, in each JRL trial, participants were passively transported to one of the four test locations around the target location. At the test location, the participant's view looked vertically down on the ground for 4 s. The fMRI analyses focused on this ground fixation period in the JRL trials in the test stage (Fig. 1b, (iii)). There were two runs, and each of the four test locations was visited 5 times in each run and each condition.

2.7.1. First level analysis

Model 1 and Model 2 served to analyze fMRI adaptation based on the distance between test locations visited successively. fMRI adaptation refers to the phenomenon that the BOLD response to the current stimulus is reduced if a similar stimulus has been presented previously, and the degree of adaptation implies the extent of overlap in neural representation between the two stimuli (Barron et al., 2016). We reasoned that as the between-location distance increases, the overlap in neural representations of test locations would decrease, and therefore neural responses would increase. An adaptation effect indicates that distance information among different locations is encoded in the neural responses (Morgan et al., 2011).

Specifically, Model 1 investigated whether the BOLD response at the currently occupied test location was parametrically modulated by its distance to the test location in the preceding trial. For each of the four conditions, a regressor modeled trials that can be modeled with parametric modulation, that is, if the visited location was not preceded by a null trial and also was not the first trial in the sequence. Therefore, this regressor consisted of trials in which the test location was preceded by the same location as well as a different location, and the parametric variable of between-location distance contained values 0 m, 2 m, 4 m, and 6 m. For each condition, a single regressor modeled trials in which the test location was preceded by a null trial or was the first trial in the sequence. Model 2 was supplementary to Model 1, in that it modeled different between-location distances with different regressors. This model was built in order to visualize the relationship between BOLD response and between-location distance, when Model 1 revealed significant adaptation.

Model 3 served to analyze effects of cue type and cue reliability on the strength of the BOLD response. Given that the navigation task used in the current study was relatively novel, it was important to determine whether this task recruited the right EC and other brain regions that are crucial for spatial navigation. Comparing correct trials and incorrect trials in activation level is a widely-used approach to infer involvement of brain regions in cognitive tasks (Chrastil et al., 2015; Pessoa et al., 2002). Therefore, we added a third factor, 'correctness', into the analysis to examine whether the right EC showed different levels of activation in correct trials vs. incorrect trials. Because some participants did not make a single mistake in some conditions within a run, scans were concatenated across the two runs in SPM12. For each of the four conditions (landmark high, landmark low, self-motion high, self-motion low), we grouped trials into correct and incorrect trials, collapsed across the four test locations. The 2 (cue type) x 2 (cue reliability) x 2 (correctness) design resulted in eight regressors.

In each of the three models, events were modelled with the default hemodynamic response function (plus time derivative) as implemented in SPM12. In addition, we included nuisance regressors that modelled head motion (three translations and three rotations), learning trials for each condition, perspective taking task prior to each block, learning trials in the compound condition, and JRL trials in the compound condition. The response phase and the feedback phase (Fig. 1b, (iv) and (v)) were not modelled to avoid a potential multicollinearity problem, because they followed immediately our event of interest, the fixation period (Fig. 1b, (iii)). In addition, the response phase and the feedback phase invoked the same cognitive processes in all four conditions, and hence it should not confound our interpretation of any condition-specific effects.

2.7.2. Second level analysis

Second level analysis was conducted to assess the results at the group level across participants. Both ROI analysis and voxel-wise analysis were conducted. In the ROI analysis, parametric estimates of the BOLD responses were averaged across all the voxels within a given ROI before being submitted to statistical tests at the group level. In the voxel-wise analysis, the parametric maps were normalized to a common space (i.e., Montreal Neurological Institute (MNI) template), and the results were examined for each voxel. Voxel-wise analysis is an important supplementary to the ROI analysis. First, the voxel-wise analysis can help verify results obtained from the ROI analysis, because ROI demarcation in the ROI analysis may contain inaccuracies. Second, the voxel-wise analysis can help localize the effects found in the ROI analysis more precisely within the ROI. Third, the voxel-wise analysis can reveal effects not detectable in the ROI analysis. It is possible that an effect is localized to a certain portion of the ROI, and the rest of the ROI could possibly wash out or cancel out the effect when the ROI is considered as a whole. Finally, whereas the ROI analysis is restricted to a certain region, the voxel-wise analysis can examine the entire brain and capture effects beyond the ROI.

2.7.2.1. Second level ROI analysis. Subject-specific beta images were not normalized. Mean BOLD responses were obtained by averaging beta estimates across voxels in the ROI. For Model 1 on distance-based adaptation, directional nonparametric permutation tests analogous to 1-tailed one-sample t tests were conducted on each of the four conditions in the two ROIs to assess whether there was evidence for positive distance-based adaptation, which would be indicative of distance coding. To control for multiple comparisons across all the eight tests (i.e., four conditions in each of the two ROIs), we implemented a nonparametric maximum-t-statistic approach, based on an established method for controlling multiple comparisons across voxels in neuroimaging studies (Nichols and Holmes, 2002; Appendix A, section 4.1).

We conducted directional statistical tests, because our primary interest was to examine whether BOLD responses decreased as the distance between locations decreased, i.e., positive adaptation. In addition, negative adaptation is difficult to interpret (Barron et al., 2016). Importantly, we conducted separate tests on individual conditions, because ANOVA models would be unable to detect adaptation effects, since they compare different conditions against each other but not a specific condition against a constant (i.e. 0). Nevertheless, given our experimental design, if significant positive adaptation was observed in any of the ROIs, we conducted a repeated measures ANOVA for the ROI with cue type and cue reliability as independent variables, to examine whether the adaptation effect was modulated by our experimental manipulations.

For Model 3, a repeated measures ANOVA was conducted with ROI (alEC vs. pmEC), cue type (landmark vs. self-motion), cue reliability (high vs. low), and correctness (correct vs. incorrect) as independent variables. Unlike Model 1, we did not conduct separate tests on the individual conditions, since the beta estimate of functional activation is interpretable only when compared between conditions.

In addition to the inferential tests, we also computed objective BFs, analogous to the behavioral analysis.

2.7.2.2. Second level voxel-wise analysis. For each participant, beta images estimated from the first-level GLMs were normalized to the MNI template. Statistical tests were conducted following the same logic of the ROI analysis described above. For Model 1 on distance-based adaptation,

we first conducted four separate nonparametric 1-tailed statistical tests on the four individual conditions (Appendix A, section 4.2), using the SPM toolbox SnPM13 (Nichols and Holmes, 2002; http://warwick.ac.uk/snpm). We then controlled for multiple comparisons across the four conditions at $p < 0.05$, with Holm-Bonferroni correction. We used this conventional multiple comparisons correction technique at this step, because currently there are no existing tools that implement the nonparametric multiple comparisons correction at both the voxel level and the condition level for MRI voxel-wise analyses. Finally, if a significant positive adaptation was observed in any of the four conditions, we examined the main effects and interaction effect in the 2 (cue type) X 2 (cue reliability) within-subjects design, to test whether the adaptation effect was modulated by experimental manipulations of cue type and cue reliability, using a nonparametric approach (Appendix A, section 4.3).

Due to our a priori hypothesis about the right EC, we tested voxels within the right EC. Small-volume correction was used to control for the family-wise type I error of multiple comparisons across voxels in this structure, using the group-level anatomical mask created from the anatomical masks of our individual participants (Appendix A, section 5). We also examined voxels beyond the right EC, with multiple comparisons controlled at $p < 0.05$ across the entire search volume and across the four conditions.

For Model 3, we tested the main effects and interaction effects in the $2 \times 2 \times 2$ within-subjects design, with cue type, cue reliability, and correctness as independent variables, using a nonparametric approach (Appendix A, section 4.3).

2.7.3. Signal dropout and signal-to-noise ratio

Large signal dropout due to susceptibility artifacts is a common problem in EC (Carr et al., 2010). The mask images generated from the first-level model estimation in SPM12 identified voxels for whom our GLMs did not explain sufficient signal variability. By comparing the anatomical masks to these mask images, we quantified signal dropout rate of the right alEC and pmEC for each participant, which equalled the number of voxels excluded from the GLM mask divided by the total number of voxels in the anatomical masks. The signal dropout rate in the right alEC ranged from 0% to 26%, with a mean of 10%. In the right pmEC, the signal dropout rate ranged from 0% to 32%, with a mean of 4%. The alEC showed greater signal loss than the pmEC ($t(21) = 2.987$, $p = 0.007$). Since no participants had signal dropout rates higher than 50%, no participants were excluded from the data analysis due to excessive entorhinal signal dropout. We also calculated temporal signal-to-noise ratio (tSNR) for the right alEC and pmEC, and found no significant differences between the two ROIs (Appendix A, section 6).

2.8. Data and code sharing

The data that support the findings of this study are available from the corresponding author, XC, upon reasonable request. The data and code sharing adopted by the authors comply with the requirements of the funding body and the ethics approval of the local ethics committee.

3. Results

3.1. Behavioural results

Behavioural results of the JRL task are shown in Fig. 3. The repeated measures ANOVA with cue type and cue reliability as independent variables (Fig. 3a) showed that both main effects were significant (cue type, $F(1,21) = 16.534$, $p = 0.001$, partial $\eta^2 = 0.434$, $BF = 0.072$; cue reliability, $F(1,21) = 48.088$, $p < 0.001$, partial $\eta^2 = 0.700$, $BF < 0.001$), meaning that participants were more accurate in the landmark conditions compared to the self-motion conditions, and that they performed better when the cue was high in reliability. The interaction effect was also significant ($F(1,21) = 18.858$, $p < 0.001$, partial $\eta^2 = 0.465$, $BF = 0.082$). Post-hoc paired t-tests revealed that the landmark high condition showed higher accuracy than the landmark low condition ($t(21) = 9.420$, $p < 0.001$, Cohen's $d = 2.008$, $BF < 0.001$); the self-motion high condition tended to be more accurate than the self-motion low condition, although the difference fell short of statistical significance ($t(21) = 1.986$, $p = 0.060$, Cohen's $d = 0.423$, $BF = 0.815$). These results indicate that the effect of cue reliability manipulation was more substantial for landmarks than self-motion cues. In brief, the results showed that the cue reliability manipulation was successful in general, in that participants performed generally better when the cue was high in reliability than when it was low in reliability. However, the cue reliability effect turned out to be more substantial for landmark cues than self-motion cues. We also calculated the mean performance across the two reliability levels for each cue type and found that the mean performance was not correlated between the two cues ($r = 0.198$, $p = 0.376$, $BF = 1.94$; Fig. 3b).

3.2. fMRI results

To reiterate, for the functional MRI data, we conducted the following two main analyses. One analysis examined adaptation effect based on the distance between the currently occupied test location and the test location in the preceding trial. The detection of an adaptation effect would indicate that spatial information (i.e., distances among locations) was encoded in the fMRI BOLD responses. The second analysis examined how the BOLD response was modulated by our experimental manipulations of cue type and cue reliability, in addition to successful navigation. In each analysis, both ROI analysis and voxel-wise analysis were conducted.

3.2.1. Distance-based adaptation

3.2.1.1. ROI analysis. To reiterate, beta estimates indicative of between-location distance adaptation were averaged across voxels in the right alEC and pmEC. First, nonparametric 1-tailed statistical tests were conducted on each of the four conditions in the two ROIs separately to assess whether there were any positive adaptation effects. If adaptation was observed in a ROI, we assessed potential differences between conditions in a repeated measures ANOVA test, with cue type and cue reliability as independent variables.

Results of the statistical tests are summarized in Table 1 and displayed in Fig. 4. In the right alEC (Fig. 4a), there was a significant positive adaptation effect in the landmark high condition ($p_{corrected} = 0.035$), and Bayes factor indicates substantial evidence favoring the alternative hypothesis ($BF = 0.124$). As shown in Fig. 4c, the mean activation in the right alEC increased linearly as the distance between successively visited locations increased. In contrast, there was no significant positive adaptation effect in the other three conditions in alEC, nor in any of the four conditions in pmEC (Fig. 4b), even at the uncorrected significance threshold. In addition, Bayes factors for the seven conditions indicated either substantial or anecdotal evidence favouring the null ($BFs > 1$). We noticed a statistical outlier in the landmark low condition (the red dot in Fig. 4a), but the pattern of results remained unchanged when we excluded this participant from the analysis.

We then analyzed the adaptation effect in a repeated measures ANOVA test for alEC, with cue type and cue reliability as independent variables. The results showed no significant effects (main effect of cue type, $F(1,21) = 0.049$, $p = 0.826$, partial $\eta^2 = 0.002$, $BF = 4.463$; main effect of cue reliability, $F(1,21) = 2.606$, $p = 0.121$, partial $\eta^2 = 0.110$, $BF = 1.628$; interaction effect, $F(1,21) = 1.547$, $p = 0.227$, partial $\eta^2 = 0.069$, $BF = 1.901$). The results remain unchanged when the outlier was excluded from the analysis (the red dot in Fig. 4a). These results suggest that the positive adaptation effect observed in the landmark high condition in alEC was not modulated by our experimental manipulations of cue type and cue reliability.

To summarize, the ROI analysis showed that the right alEC showed positive distance-based adaptation in the landmark high condition, in

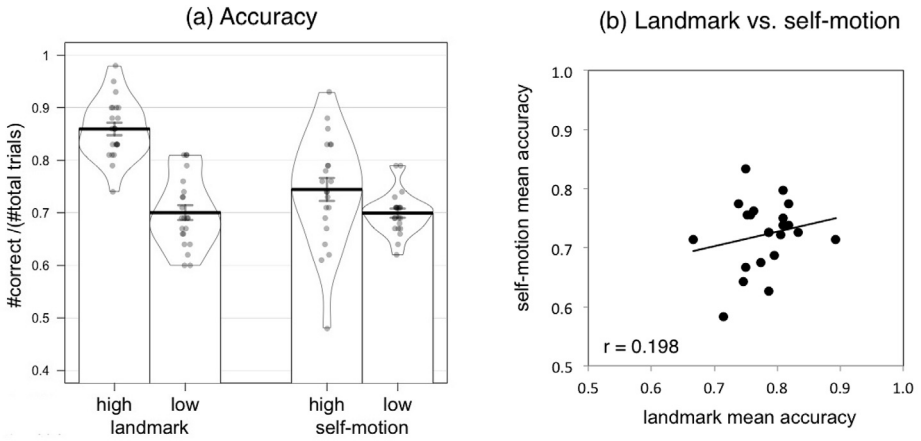

Fig. 3. Behavioral results. (a), accuracy in the judgment of relative location (JRL) task is plotted as a function of cue type (landmark vs. self-motion) and cue reliability (high vs. low), with individual data points plotted as gray dots. The bar height represents mean of the data; error bars represent S.E. of the mean; curved shapes represent smoothed density of the data. The plot was generated using the 'pirateplot' function in the 'yarrr' package installed in R (Nathaniel Phillips, 2017). (b), scatterplot between mean accuracy in the landmark conditions and in the self-motion conditions. The straight line represents the best fit of the linear regression. Pearson correlation (r) is displayed.

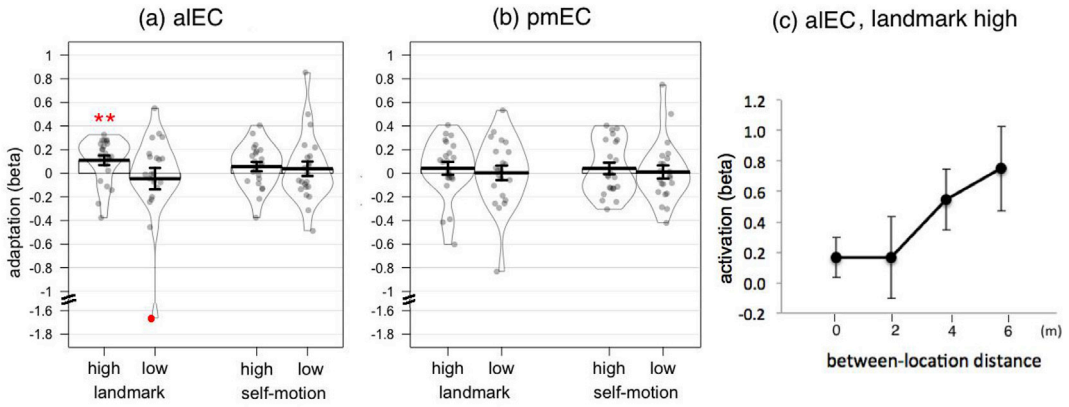

Fig. 4. ROI analysis of distance-based adaptation. The adaptation effect is plotted as a function of cue type (landmark vs. self-motion) and cue reliability (high vs. low) for the right anterior-lateral entorhinal cortex (alEC, (a)) and the right posterior-medial entorhinal cortex (pmEC, (b)). Individual data points are plotted as gray dots. The statistical outlier is highlighted as a red dot (<1st quartile - 3 interquartile range). The bar height represents mean of the data; error bars represent S.E. of the mean; curved shapes represent smoothed density of the data. ** means $p_{uncorrected} < 0.01$. (c), mean activation of the right alEC is plotted as a function of between-location distance in the landmark high condition. Error bars represent S.E. of the mean.

that its activation level increased linearly as the between-location distance increased. However, this adaptation effect was not modulated by our experimental manipulations of cue type and cue reliability. We did not observe significant adaptation effects in any of the other three conditions in alEC or any of the four conditions in pmEC.

3.2.1.2. Voxel-wise analysis. To localize the distance coding within EC more precisely, to test for adaptation effects that might have been missed in the ROI analysis, and to test for adaptation effects outside our ROIs, we conducted voxel-wise analysis, following the same logic of the statistical testing in the ROI analysis. The results are summarized in Table 2 and Fig. 5.

One-tailed nonparametric statistical tests for the four individual conditions revealed a positive adaptation in the landmark high condition in the right EC (Figure 5a.1; peak $t_{21} = 5.36$, $p_{FWE\text{-}corrected} = 0.011 < \alpha = 0.05/3 = 0.017$). Notably, the peak voxel also represents the highest level of statistical significance in the entire search volume. Comparing our results with the alEC-pmEC border in MNI space in Maass et al. (2015), we found that the peak voxel is within the alEC mask, albeit very close to the border (Fig. 5, middle in the upper row). The mean adaptation effect around the peak voxel was high in the landmark high condition, but close to 0 in all the other three conditions (Fig. 5a2). The mean BOLD response around the peak voxel in the landmark high condition increased in a linear manner as between-location distance increased (Fig. 5a3). No significant positive adaptation effects were observed outside of the right EC in the landmark high condition.

Table 2
Voxel-wise analysis of distance-based adaptation. Results were corrected for multiple comparisons at $p < 0.05$ across voxels within the right entorhinal cortex (EC) and across the four conditions. Listed are condition, MNI coordinates, T values, and corrected p values (α with a family-wise type I error of 0.05) of the peak voxel, along with cluster size at $p_{uncorrected} < 0.01$ within the right EC. Only significant effects are listed.

Condition	Coordinates (x, y, z, in mm)	Voxel level (T-score)	$p_{FWE\text{-}corrected}$	α	Cluster size
Landmark high	17, −7, −27	5.36	0.011	0.05/3	92
Self-motion high	26, −22, −27	5.74	0.006	0.05/4	139

One-tailed nonparametric statistical tests also revealed a positive adaptation effect in the self-motion high condition in the right EC (Fig. 5b1; peak $t_{21} = 5.74$, $p_{FWE\text{-}corrected} = 0.006 < \alpha = 0.05/4 = 0.013$). Comparing our results with the alEC-pmEC border in MNI space in Maass et al. (2015), we found that the peak voxel is within the pmEC mask, and is also at a distance from the border (Fig. 5, middle in the upper row). The mean adaptation around the peak voxel was high in the self-motion high condition and close to 0 in the other three conditions (Fig. 5b2). More

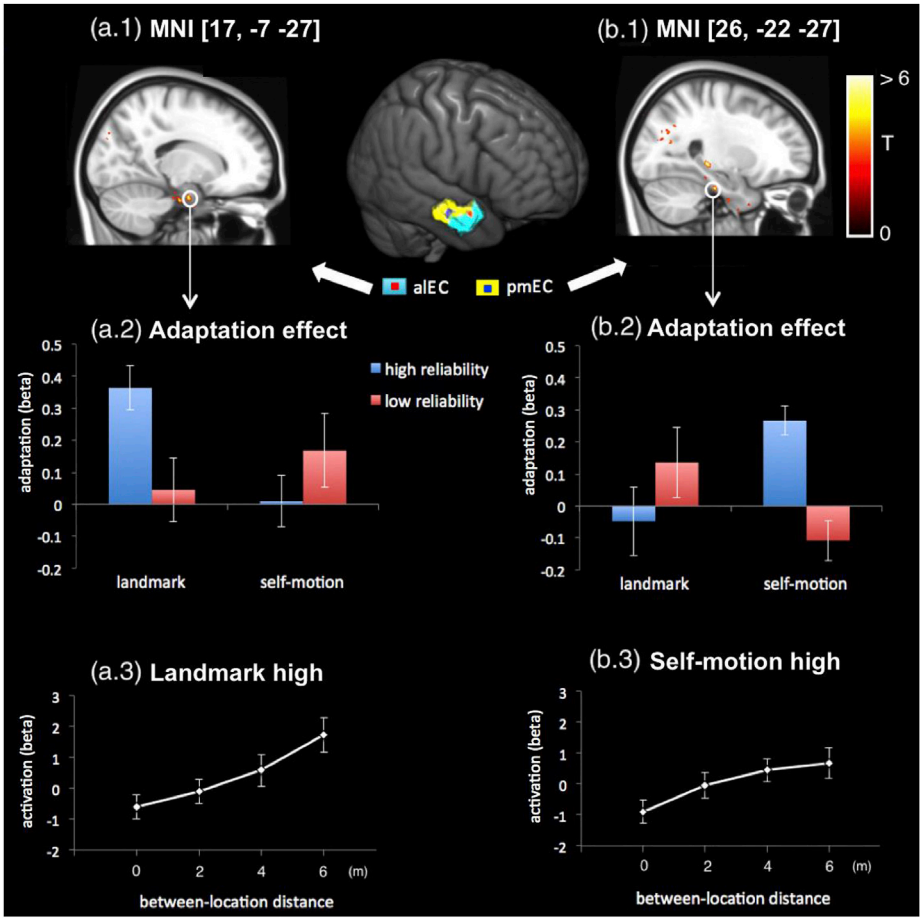

Fig. 5. Voxel-wise analysis of distance-based adaptation. The right entorhinal cortex (EC) showed positive adaptation in the landmark high condition (left column, a.1 to a.3) and the self-motion high condition (right column, b.1 to b.3). In the upper row (a.1 & b.1), to show sub-threshold voxels, results are displayed on the MNI template at a threshold of $p_{uncorrected} < 0.01$ (i.e., $t > 2.518$), with MNI coordinates of the peak voxels indicated. Shown in the middle is the normalized group anatomical mask for the right EC, rendered in the 3D skull-stripped MNI template, with the alEC-pmEC border copied from Maass et al. (2015). The red blob within alEC (in cyan) and the blue blob within pmEC (in yellow) represent the clusters (thresholded at $p_{uncorrected} < 0.01$) showing distance-based adaptation in the landmark high condition (left column) and the self-motion high condition (right column), respectively. To visualize the results, we created 2-mm-radius spheres around the peak voxels (Brett et al., 2002), and then extracted the beta estimates within the spheres. In the middle row (a.2 & b.2), mean beta estimates of adaptation are plotted as a function of cue type (landmark vs. self-motion) and cue reliability (high vs. low). In the lower row (a.3 & b.3), mean beta estimates of BOLD response strength are plotted as a function of between-location distance. Error bars represent ±S.E. of the mean.

specifically, the mean BOLD response increased linearly as the between-location distance increased in the self-motion high condition (Fig. 5b3). Beyond EC, we also observed a tendency for positive adaptation in the self-motion high condition in the right fusiform cortex, which was marginally significant with multiple comparisons correction across conditions (peak $t_{21} = 7.25$, $p_{FWE\text{-}corrected} = 0.019 < \alpha = 0.10/4 = 0.025$, MNI coordinate [43, −36, −26]). We did not observe any significant positive adaptation effects in the landmark low condition and the self-motion low condition, neither within nor outside the right EC.

To examine whether the observed positive adaptation effects were modulated by the experimental manipulations, we conducted nonparametric statistical tests analogous to the repeated measures ANOVA test, with cue type and cue reliability as the independent variables. In the right EC, there were no significant main effects ($ps_{FWE\text{-}corrected} > 0.10$, 2-tailed), and no significant interaction effect ($ps_{FWE\text{-}corrected} > 0.07$, 2-tailed). No significant effects were observed outside of the right EC.

To summarize, the voxel-wise analysis showed that the right EC adapted to between-location distance for both landmark and self-motion cues when they were relatively high in reliability, but the effect was localized in different entorhinal subregions for different cues. Specifically, alEC showed distance-based adaptation for landmark cues, consistent with the ROI analysis; on the contrary, pmEC showed distance-based adaptation for self-motion cues, which was not revealed by the ROI analysis. Consistent with the ROI analysis, the adaptation effects were not modulated by cue type or cue reliability.

3.2.1.3. Control analysis. To verify the validity of the abovementioned findings on distance-based adaptation, we investigated whether they could be explained by confounding factors. Detailed statistics of the control analysis corresponding to each factor can be found in the supplementary materials (Appendix A, section 7). To preview, we did not find evidence that any of these factors could explain the distance-based adaptation effects.

3.2.1.3.1. Passive movement. In the JRL task, the ground fixation period – which was used to assess distance coding – was preceded by a passive movement, during which the sensory inputs differed among the four conditions. Given the slow temporal dynamics of the hemodynamic response, it is possible that the distance-based adaptation effect measured at the ground fixation period could have reflected effects in the passive movement stage. To investigate this confound, we created a GLM corresponding to Model 1 (section 2.7.1), but with passive movement modelled. We found that the pattern of results remained unchanged, which is expected given the negligible correlations between the parametric regressors modelling the distance-based adaptation effects and the regressors modelling the passive movement phases ($|rs| < 0.06$). This indicates that the observed distance-based adaptation effects were not confounded by the movement phase immediately preceding the ground fixation period.

3.2.1.3.2. Temporal distance. Unlike a typical fMRI adaptation paradigm (e.g., Morgan et al., 2011), the temporal interval between two successively visited locations in the JRL task varied across trials, due to the fact that the travelled distances to the four test locations were different, that the starting position varied from trial to trial in the landmark conditions, and that the movement speed was randomized from trial to trial. Since neural adaptation is particularly sensitive to the temporal delay (Barron et al., 2016), it is possible that the distance-based adaptation effects observed in the landmark high condition and the self-motion high condition were caused by a general adaptation to location occupation that was modulated by the temporal delay. We

correlated temporal intervals and spatial distances between successively visited locations across trials for each condition and each participant. The two variables were not significantly correlated in any condition, and the magnitude of the mean correlation was very low ($|rs| < 0.06$, $ps > 0.08$). Nevertheless, we performed the same adaptation analysis with temporal interval as the parametric modulator. This analysis revealed no significant adaptation effects based on temporal distance in the landmark high condition or the self-motion high condition in the right alEC, where significant spatial-distance-based adaptation effects were observed. Unexpectedly, the ROI analysis revealed marginally significant temporal-interval-based adaptation effects in the right alEC in the two low reliability conditions ($ps_{corrected} < 0.10$). While it is difficult to interpret the potential temporal-interval-based adaptation effects in the two low-reliability conditions, these results suggest that the spatial-distance-based adaptation effects observed in the two high reliability conditions reflected neural coding of spatial distance instead of temporal distance between successively visited locations.

3.2.1.3.3. Response adaptation. Given our experimental design, smaller between-location distances also contained a larger proportion of trials in which the correct response was the same between the current trial and the preceding trial. Given that a given correct answer (i.e., 'ahead'/'behind') was always associated with the same motor movement (i.e., pulling the front/back button), the observed distance-based adaptation effects could have been confounded by response adaptation effect, i.e. the BOLD response was reduced when the response in the current trial was the same as in the preceding trial (compared to when it was different). To address this question, we created a GLM that modelled 'same' correct responses and 'different' correct responses in separate regressors. We did not find any significant response adaptation effects, except for a marginally significant response adaptation in the landmark high condition revealed in the voxel-wise analysis, at a site very close to the alEC-pmEC border (Fig. 5, middle in the upper row). The pattern of results remained unchanged when we modelled participants' actual responses instead of correct responses. Given that response adaptation should be present across conditions, these results strongly suggest that the distance-based adaptation in EC was not confounded by a potential response adaptation.

3.2.1.3.4. Behavioral accuracy. Overall, participants performed better with landmarks than self-motion cues, which is in line with previous behavioral findings that humans are relatively poor in path integration (Loomis et al., 1993), especially when body-based cues are absent and only visual optic flow is available (Campos et al., 2010; Kearns et al., 2002; Ruddle and Lessels, 2006, 2009), as in our case. In particular, performance was better in the landmark high condition than the self-motion high condition ($p < 0.001$), where significant distance-based adaptation effects were observed. Therefore, any differences in adaptation effect between the two conditions could have been confounded by behavioral accuracy. To address this issue, we analyzed adaptation effects only for correct trials in each condition. Crucially, whenever there were more correct trials in the landmark high condition than in the self-motion high condition, we randomly selected a subset of the trials in the landmark high condition so that its total number of trials did not exceed that in the self-motion high condition. The results remained unchanged, except that the distance-based adaptation effect in the self-motion high condition in the voxel-wise analysis became marginally significant, and that there was now a marginally significant distance-based adaptation effect in the landmark low condition at a coordinate adjacent to the distance-based adaptation effect observed in the landmark high condition. These results suggest that the differential distance-based adaptation effects observed between landmarks and self-motion cues were not confounded by the unmatched levels of behavioral accuracy.

3.2.2. Effects of cue type, cue reliability, and successful navigation

Here, we investigated how the strength of the BOLD response was modulated by our experimental manipulations and successful navigation. Both ROI analysis and voxel-wise analysis were conducted.

3.2.2.1. ROI analysis. To reiterate, the mean neural response was analyzed in a repeated measures ANOVA with ROI, cue type, cue reliability, and correctness as independent variables. Results are summarized in Table 3 and displayed in Fig. 6.

The main effect of correctness was significant ($p = 0.007$, $BF = 0.058$). No significant interaction effects were significant ($ps > 0.1$), indicating that the effect of successful navigation was comparable between the ROIs and was independent of cue type and cue reliability. As shown in Fig. 6, both alEC and pmEC were more activated in correct trials than in incorrect trials. Notably, this pattern existed in every combination of cue type and cue reliability in both ROIs. Interestingly, the main effect of ROI was significant ($p < 0.001$, $BF < 0.001$); as shown in Fig. 6, alEC was more activated than pmEC. The results remained largely unchanged when we excluded the two outliers from the analysis (red dots in Fig. 6), except that the three-way interaction cue*reliability*correctness became significant ($p = 0.030$). Since the pattern of stronger activation in correct trials than incorrect trials still existed in every condition in both ROIs, this interaction effect does not affect our interpretation of the main effect of successful navigation.

To summarize, we found that the entire right EC was more activated when the trial was completed correctly than when it was failed. We also found that alEC was more activated than pmEC in general.

3.2.2.2. Voxel-wise analysis. Results of the voxel-wise analysis are displayed in Table 4 and Fig. 7. Within the right EC, we observed a cluster showing main effect of correctness, which was driven by stronger activation in correct trials than incorrect trials. Beyond the right EC, we observed a main effect of correctness in the right hippocampus and in the left precuneus. The hippocampus and the precuneus were more activated in correct trials than incorrect trials. We did not observe significant

Table 3
Effects of ROI, cue type, cue reliability, and correctness on the strength of the BOLD response in the ROI analysis, as examined in a repeated measures ANOVA. Results without the statistical outliers are listed in parentheses. Significant effects are highlighted in bold.

Effect	F	p	Partial η^2	BF
ROI	**29.749 (25.451)**	**< 0.001 (< 0.001)**	**0.586 (0.573)**	**< 0.001 (< 0.001)**
Cue	0.316 (2.205)	0.580 (0.154)	0.015 (0.104)	6.226 (1.373)
Reliability	2.138 (3.670)	0.159 (0.071)	0.092 (0.162)	2.919 (1.280)
Correctness	**8.759 (13.336)**	**0.007 (0.002)**	**0.294 (0.412)**	**0.058 (0.062)**
ROI * cue	<0.001 (0.019)	0.990 (0.893)	<0.001 (0.001)	6.161 (6.008)
ROI * reliability	1.489 (1.163)	0.236 (0.294)	0.066 (0.058)	3.928 (3.871)
Cue * reliability	0.149 (0.240)	0.704 (0.630)	0.007 (0.012)	3.492 (5.297)
ROI * cue * reliability	0.383 (0.699)	0.543 (0.414)	0.018 (0.035)	4.218 (3.680)
ROI * correctness	1.360 (2.092)	0.257 (0.164)	0.061 (0.099)	5.094 (4.330)
Cue * correctness	0.009 (0.162)	0.927 (0.692)	<0.001 (0.008)	6.057 (5.330)
ROI* cue * correctness	0.880 (0.554)	0.359 (0.466)	0.040 (0.028)	4.006 (3.884)
Reliability * correctness	0.013 (0.018)	0.912 (0.894)	0.001 (0.001)	6.099 (5.831)
ROI * reliability * correctness	1.844 (2.82)	0.189 (0.109)	0.081 (0.129)	4.066 (3.407)
Cue * reliability * correctness	0.847 **(5.525)**	0.368 **(0.030)**	0.039 **(0.225)**	2.872 **(0.577)**
ROI * cue * reliability * correctness	2.608 (1.940)	0.121 (0.180)	0.110 (0.093)	2.474 (2.539)

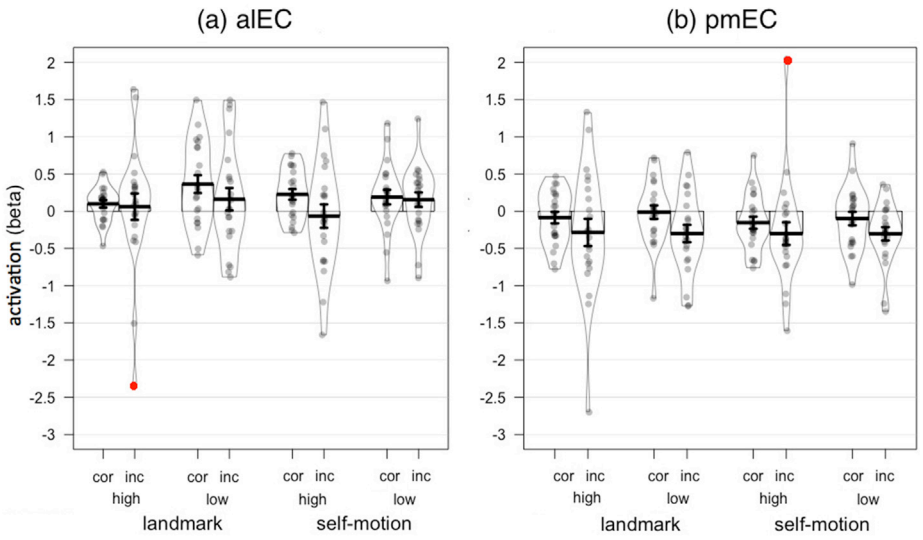

Fig. 6. Effects of successful navigation in the ROI analysis. The right anterior-laterial entorhinal cortex (alEC, (a)) and posterior-medial entorhinal cortex (pmEC, (b)) were more activated in correct trials ('cor') than incorrect trials ('inc'), regardless of cue type (landmark vs. self-motion) and cue reliability (high vs. low). Gray dots represent individual data points. Statistical outliers are highlighted as red dots (<1st quartile - 3 * interquartile range or > 3rd quartile + 3 * interquartile range). The bar height represents mean of the data; error bars represent S.E. of the mean; curved shapes represent smoothed density of the data.

effects of cue type, cue reliability, or interactions within or beyond the right EC.

3.2.2.3. Control analysis. We observed that the right EC, the hippocampus, and the precuneus were more activated in correct trials than in incorrect trials. To verify the validity of these findings, we evaluated whether they were confounded by confounding factors, i.e., passive movement, trial difficulty, and unequal numbers of trials. We did not find evidence that the observed effect of successful navigation could be explained by any of these factors. Detailed description of the control analysis is in the supplementary materials (Appendix A, section 8).

Table 4
Effects of successful navigation in the voxel-wise analysis. Listed are region, MNI coordinates, T-values, and corrected p-values of the peak voxel (2-tailed), along with cluster size at $p_{uncorrected} < 0.001$ (1-tailed). To control for multiple comparisons at $p < 0.05$, small volume correction (based on the right EC mask) was performed for EC, and correction based on the entire search volume was performed for voxels outside EC. Only significant effects are listed. LH stands for left hemisphere, and RH stands for right hemisphere.

region	Coordinates		Voxel level (T)	$p_{FWE\text{-}corrected}$	Cluster size
	LH	RH			
Small volume correction within ROI					
Right EC		18, −11, −22	5.24	0.020	7
		16, −2, −26	4.66	0.076	19
Entire volume correction					
Hippocampus		36, −11, −23	8.18	0.008	43
		32, −28, −10	8.16	0.008	167
Precuneus	−12, −56, 24		7.39	0.010	4098
	−9, −55, 24		6.98	0.022	
	−3, −51, 18		6.94	0.048	
	−2, −56, 19		6.92	0.096	
	−6, −52, 20		6.82	0.084	
		8, −49, 23	6.89	0.078	

4. Discussion

We examined how subregions of the human entorhinal cortex support landmark-based navigation and path integration, using virtual reality and ultra-high field fMRI at 7T. In a novel navigation task, we dissociated self-motion cues and landmark cues and manipulated their reliability levels. Distance-based fMRI adaptation analysis revealed that the right alEC encoded between-location distance when landmark cues relatively high in reliability were used, whereas the right pmEC encoded between-location distance based on self-motion cues relatively high in reliability. However, in contrast to the significant effects of cue type and cue reliability observed in the behavioral data, distance-based adaptation was not modulated by these experimental manipulations. We also found that both alEC and pmEC, along with the hippocampus and the precuneus, were involved in successful navigation by showing stronger activation in correct trials than in incorrect trials. Together, our study has provided the first evidence for distance coding in different entorhinal subregions for different cue types.

Using our newly developed navigation task, we found that participants' behavioral performance was not correlated between the landmark conditions and the self-motion conditions. This finding is consistent with previous behavioral studies demonstrating a relative independence of landmark-based navigation and path integration in both rodents (Shettleworth and Sutton, 2005) and humans (Chen et al., 2017), and it indicates that our experimental manipulation of cue dissociation was successful. In addition, our participants also reported distinct strategies associated with landmarks (e.g., matching the perceived size of the landmark) and self-motion cues (e.g., estimating the travelled distance based on movement speed). The relative independence of the two navigation processes can be explained by the fact that they involve distinct cognitive processes, namely discrete positional computations vs. continuous integration of spatial information (Etienne et al., 1996; Mittelstaedt and Mittelstaedt, 1980).

In line with our behavioral results, the most important fMRI finding of our study is that the right alEC and the right pmEC encoded spatial distances between locations based on landmarks and self-motion cues, respectively, as revealed by the analysis of distance-based adaptation. It is worth noting that in our task, participants never travelled directly from one test location to another, although they passed through in-between test locations when travelling to those farther away from the starting position of the movement. Representing distances among the test locations in our task, therefore, to some extent required participants to infer novel spatial relations from experienced spatial relations, a critical ability

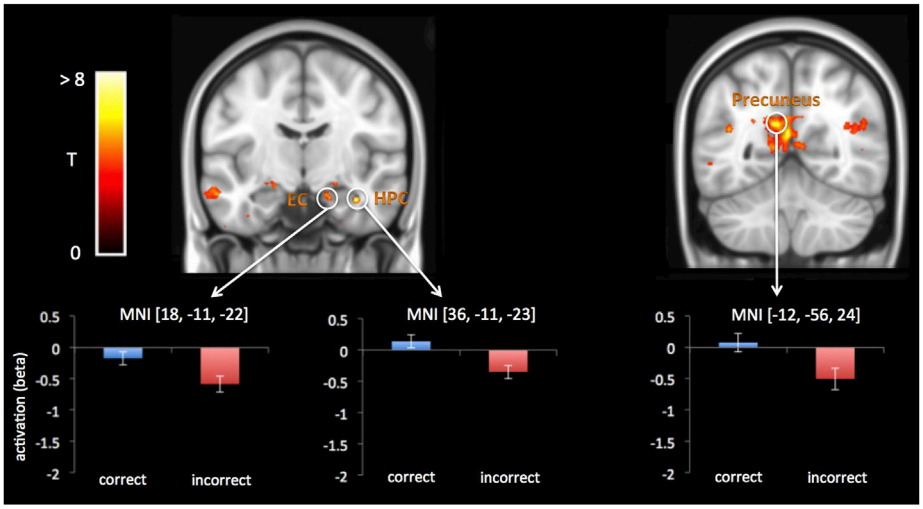

Fig. 7. Effects of successful navigation in the voxel-wise analysis. Within the ROI, the right entorhinal cortex (EC) exhibited stronger activation in correct trials than incorrect trials. Beyond EC, the right hippocampus (HPC) and left precuneus were also more activated in correct trials than in incorrect trials. In the upper row, to show sub-threshold voxels, results are displayed on the MNI template at a threshold of $p_{uncorrected} < 0.001$ (i.e., $t > 3.527$). We created spheres of 2 mm in radius around the peak voxels (highlighted in white circles) and extracted mean beta estimates (Brett et al., 2002). In the bottom row, mean beta estimates of BOLD response strength are plotted as a function of correctness (correct vs. incorrect), with MNI coordinates of the peak voxels indicated. Error bars represent SE of the mean.

for building a 'cognitive map' of the environment (Tolman, 1948). Therefore, distance coding in the human EC might provide a neural mechanism of constructing a 'cognitive map' in a one-dimensional linear space during navigation.

Our study also offers the first empirical evidence from human spatial navigation to shed light on the functional segregation within EC. Based on rodent findings, the content-based view proposes that the functional segregation depends on the type of spatial information; specifically, the rodent LEC and MEC specialize in spatial processing related to local landmarks and self-motion cues, respectively (Knierim et al., 2014). Recent studies have shown that neurons recorded in LEC display spatial modulations to local landmarks (Deshmukh and Knierim, 2011; Wang et al., 2018), which could provide a neuronal mechanism for the landmark-related distance coding in the human alEC (the functional homolog to the rodent LEC; Maass et al., 2015; Schröder et al., 2015) observed in our study. In contrast, grid cells in the rodent MEC, with their remarkably regular and relatively context-invariant multi-field firings (Hafting et al., 2005), may provide a universal spatial metric for path integration (McNaughton et al., 2006; Moser and Moser, 2008), probably based on speed signals generated in speed cells (Kropff et al., 2015). Confirming this speculation, recent studies showed that MEC lesions caused deficits in path integration on linear tracks (Jacob et al., 2017), that disrupted grid cell firing in MEC caused path integration deficits (Gil et al., 2018), and that behavioral bias in human path integration corresponded to grid cell firing properties (Chen et al., 2015). Our findings are consistent with these observations and provide critical evidence for the involvement of the human pmEC (the functional homolog to the rodent MEC; Maass et al., 2015; Schröder et al., 2015) in path integration. While also consistent with a recent human fMRI study showing that grid-cell-like activation in the entire human EC predicted individual path integration abilities in older adults (Stangl et al., 2018), our results suggest that this relationship might be mainly driven by grid-cell-like activation in pmEC.

In contrast, our findings are only partially consistent with the conventional hypothesis that the rodent LEC (or human alEC) specializes in object-related nonspatial processing and the rodent MEC (or human pmEC) in spatial processing (Witter, 1993; Witter et al., 2017). On the one hand, while the observed distance coding for path integration demonstrates spatial coding in pmEC, we did not observe distance coding in pmEC for landmarks. As a consequence, pmEC may not be involved in any type of spatial computations but might be dedicated to the processing of self-motion information. On the other hand, while the landmark-related distance coding in alEC confirms its sensitivity to landmark objects (Chao et al., 2016; Wilson et al., 2013), our findings suggest that alEC can also compute fine-grained spatial distance information. In addition to recent studies showing neurons spatially tuned to local objects in the rodent LEC (Knierim et al., 2014; Wang et al., 2018), our findings also resonate with studies demonstrating an important role of the rodent LEC in spatial learning (Kuruvilla and Ainge, 2017). However, the findings on spatial sensitivity of LEC neurons have been inconsistent, which we speculate might be related to whether and to what extent local objects are utilized for navigational purposes. In studies where spatial specificity was sparse in LEC, there were either no (Yoganarasimha et al., 2011) or very few (Hargreaves et al., 2005) local landmarks, whereas such cues were plenty in studies where object-related spatial specificity in LEC was observed (Deshmukh and Knierim, 2011; Wang et al., 2018). In addition, behavioral studies have frequently shown that the navigational use of local objects is often overshadowed or blocked by other environmental cues, e.g., distal landmarks (Diez-Chamizo et al., 1985) and geometric cues (Cheng, 1986; Doeller and Burgess, 2008; Wilson and Alexander, 2008), which might explain why it seems relatively rare to observe local-object-related spatial specificity in LEC. Together, these findings call for more detailed analyses of how spatial and nonspatial computations might be organized in the medial temporal lobe.

Human fMRI studies have also shown a nonspatial vs. spatial differentiation between alEC and pmEC. Specifically, similar to the connectivity pattern observed in rodents (Witter et al., 2017), the human alEC is functionally connected with the perhirhinal cortex and its related anterior-temporal cortical system, which is linked to nonspatial object processing, whereas pmEC is functionally connected with the parahippocampal cortex and its related posterior-medial cortical system, which is linked to spatial processing (Maass et al., 2015; Schröder et al., 2015). In addition, alEC is more activated in nonspatial tasks with objects (Reagh and Yassa, 2014; Schröder et al., 2015) and faces (Schultz et al., 2012), whereas pmEC is more activated in spatial tasks with scenes (Schröder et al., 2015) and spatial locations (Reagh and Yassa, 2014), although there is some overlap between the nonspatial and spatial processing within EC (Berron et al., 2018). Critically, our experiment differs from these studies in many aspects, e.g., general episodic memory vs. spatial memory, passive picture viewing vs. real navigation. Accordingly, it is difficult to compare our findings to these studies, but they provide critical evidence from the domain of human spatial navigation that alEC and pmEC support landmark-based navigation and path integration, respectively.

Two recent studies showed that in rodents, both LEC and MEC encoded spatial information in relation to external environmental cues, but in different reference frames (Høydal et al., 2019; Wang et al., 2018). Specifically, while neurons in LEC encoded egocentric bearings of external objects, neurons in MEC represented allocentric bearings of

external objects. In addition, LEC and MEC neurons also encoded geometric boundaries in the egocentric and allocentric reference frames, respectively (Wang et al., 2018). Moreover, these studies also observed distance tuning in both LEC (Wang et al., 2018) and MEC (Høydal et al., 2019) in relation to local objects. Importantly, the distance coding we observed in both alEC and pmEC reflected distances among different spatial locations, which is allocentric or at least nonegocentric (Klatzky, 1998). As a consequence, a simple differentiation of egocentric vs. allocentric representations may be insufficient to characterize the functional segregation of EC. To address this question, future investigations would need to employ a full factorial design that manipulates both cue type and reference frame, an extension of our paradigm to angular estimation, and a differentiation between different environmental cues (i.e., local landmarks vs. geometric boundaries).

Similar to our work, several studies have used fMRI adaptation (Morgan et al., 2011) and multivoxel pattern analysis (Deuker et al., 2016; Nielson et al., 2015) to demonstrate distance coding among landmarks in the human hippocampus. By contrast, we did not observe this effect in the hippocampus, even when we applied the same statistical thresholds as used in the right EC. However, we noticed a cluster of voxels in the right thalamus that showed some degree of distance-based adaptation in the self-motion high condition that would survive the threshold applied to the right EC (see Fig. 5b1). This cluster extended to voxels in the hippocampal tail at $p_{uncorrected} < 0.01$. The cluster of voxels in alEC showing distance-based adaptation effect in the landmark-high condition also extended to the hippocampus at $p_{uncorrected} < 0.01$ (Fig. 5a1). Overall, the evidence for the hippocampal involvement in distance coding in our study is relatively weak. The discrepancy between our study and previous studies could be related to different experimental setups (e.g., navigation vs. picture-viewing, new vs. well-learned environment). Another possibility is that the hippocampus might be involved in spatial coding only when both landmarks and self-motion cues are utilized in navigation. In the previous studies, participants' mental representation of the environment had been formed through free or guided exploration and should have had contributions from both landmarks and self-motion cues (Gallistel, 1990; Wang, 2016). By contrast, these two cue types were clearly dissociated in the single-cue trials analyzed in our study. Consistent with our speculation, rodent studies have shown disrupted positional coding of hippocampal place cells when either LEC inputs or MEC inputs were eliminated (Lu et al., 2013; Brun et al., 2008), suggesting that an intact spatial representation in the hippocampus requires projections from both entorhinal subregions.

Finally, we found that the right EC, hippocampus, and precuneus were involved in successful navigation for both path integration and landmark-based navigation. These findings are consistent with previous studies demonstrating a prominent role of these structures in spatial navigation (Moser et al., 2008; Schindler and Bartels, 2013; Wolbers et al., 2008). In particular, our results are consistent with previous findings that hippocampal activation covaried with trial-by-trial fluctuations in path integration accuracy (Chrastil et al., 2015; Sherrill et al., 2013; Wolbers et al., 2007). The involvement of these structures in successful navigation could be attributed to attentional modulation; that is, more attention to spatial inputs could have enhanced the engagement of navigation-related brain regions, which in turn led to better navigation performance. Attentional modulation of hippocampal place fields has been observed in rodents (Kentros et al., 2004), but it is currently unknown whether similar effects are present in EC. The involvement of brain regions critical for spatial navigation (i.e., EC, hippocampus and precuneus) also suggests that the novel task we developed in the current study engaged the core neural system of spatial navigation, despite the simple navigation task and the sparse virtual environment.

5. Conclusions

To conclude, using a novel navigation task, we found that different entorhinal subregions encoded distance information derived from landmarks and self-motion cues. Our findings advance the understanding of how the EC supports different navigation modes, and they call for a reconceptualization of the labor division between different entorhinal subregions in processing different spatial cues. Our study also opens the door for future work to examine the neural mechanisms of cue interaction in spatial navigation.

Acknowledgements

This research was supported by a research grant from the Human Frontiers Science Program (RGP 0062/2014, awarded to T.W.).

Appendix A. Supplementary data

Supplementary data to this article can be found online at https://doi.org/10.1016/j.neuroimage.2019.116074.

References

Abrahams, S., Pickering, A., Polkey, C.E., Morris, R.G., 1997. Spatial memory deficits in patients with unilateral damage to the right hippocampal formation. Neuropsychologia 35 (1), 11–24.
Aguirre, G.K., 2007. Continuous carry-over designs for fMRI. Neuroimage 35 (4), 1480–1494.
Aguirre, G.K., Mattar, M.G., Magis-Weinberg, L., 2011. de Bruijn cycles for neural decoding. Neuroimage 56 (3), 1293–1300.
Barron, H.C., Garvert, M.M., Behrens, T.E., 2016. Repetition suppression: a means to index neural representations using BOLD? Philos. Trans. R. Soc. B 371 (1705), 20150355.
Bates, S.L., Wolbers, T., 2014. How cognitive aging affects multisensory integration of navigational cues. Neurobiol. Aging 35 (12), 2761–2769.
Berron, D., Vieweg, P., Hochkeppler, A., Pluta, J., Ding, S.-L., Maass, A., et al., 2017. A protocol for manual segmentation of medial temporal lobe subregions in 7 Tesla MRI. Neuroimage: Clinic 15, 466–482.
Berron, D., Neumann, K., Maass, A., Schütze, H., Fliessbach, K., Kiven, V., et al., 2018. Age-related functional changes in domain-specific medial temporal lobe pathways. Neurobiol. Aging 65, 86–97.
Brett, M., Anton, J.-L., Valabregue, R., Poline, J.-B., 2002. Region of interest analysis using the MarsBar toolbox for SPM 99. Neuroimage 16 (2), S497.
Brun, V.H., Leutgeb, S., Wu, H.-Q., Schwarcz, R., Witter, M.P., Moser, E.I., Moser, M.-B., 2008. Impaired spatial representation in CA1 after lesion of direct input from entorhinal cortex. Neuron 57 (2), 290–302.
Campos, J.L., Byrne, P., Sun, H., 2010. The brain weights body-based cues higher than vision when estimating walked distances. Eur. J. Neurosci. 31 (10), 1889–1898.
Carr, V.A., Rissman, J., Wagner, A.D., 2010. Imaging the human medial temporal lobe with high-resolution fMRI. Neuron 65 (3), 298–308.
Chao, O.Y., Huston, J.P., Li, J., Wang, A., de Souza Silva, M.A., 2016. The medial prefrontal cortex-lateral entorhinal cortex circuit is essential for episodic-like memory and associative object-recognition. Hippocampus 26 (5), 633–645.
Chen, X., He, Q., Kelly, J.W., Fiete, I.R., McNamara, T.P., 2015. Bias in human path integration is predicted by properties of grid cells. Curr. Biol. 25 (13), 1771–1776.
Chen, X., McNamara, T.P., Kelly, J.W., Wolbers, T., 2017. Cue combination in human spatial navigation. Cogn. Psychol. 95, 105–144.
Cheng, K., 1986. A purely geometric module in the rat's spatial representation. Cognition 23 (2), 149–178.
Chrastil, E.R., Sherrill, K.R., Aselcioglu, I., Hasselmo, M.E., Stern, C.E., 2017. Individual differences in human path integration abilities correlate with gray matter volume in retrosplenial cortex, hippocampus, and medial prefrontal cortex. ENeuro 4 (2). ENEURO.0346-16.2017.
Chrastil, E.R., Sherrill, K.R., Hasselmo, M.E., Stern, C.E., 2015. There and back again: Hippocampus and retrosplenial cortex track homing distance during human path integration. J. Neurosci. 35 (46), 15442–15452.
Deshmukh, S.S., Knierim, J.J., 2011. Representation of non-spatial and spatial information in the lateral entorhinal cortex. Front. Behav. Neurosci. 5, 69.
Deuker, L., Bellmund, J.L., Schröder, T.N., Doeller, C.F., 2016. An event map of memory space in the hippocampus. ELife 5, e16534.
Diez-Chamizo, V., Sterio, D., Mackintosh, N., 1985. Blocking and overshadowing between intra-maze and extra-maze cues: a test of the independence of locale and guidance learning. Q. J. Exp. Psychol. 37 (3b), 235–253.
Doeller, C.F., Barry, C., Burgess, N., 2010. Evidence for grid cells in a human memory network. Nature 463 (7281), 657–661.
Doeller, C.F., Burgess, N., 2008. Distinct error-correcting and incidental learning of location relative to landmarks and boundaries. Proc. Natl. Acad. Sci. U.S.A. 105 (15), 5909–5914.
Doeller, C.F., King, J.A., Burgess, N., 2008. Parallel striatal and hippocampal systems for landmarks and boundaries in spatial memory. Proc. Natl. Acad. Sci. U.S.A. 105 (15), 5915–5920.
Etienne, A.S., Jeffery, K.J., 2004. Path integration in mammals. Hippocampus 14 (2), 180–192.

Etienne, A.S., Maurer, R., Séguinot, V., 1996. Path integration ln mammals and its interaction with visual landmarks. J. Exp. Biol. 199 (1), 201–209.
Etienne, A.S., Maurer, R., Berlie, J., Reverdin, B., Rowe, T., Georgakopoulos, J., Séguinot, V., 1998. Navigation through vector addition. Nature 396 (6707), 161–164.
Etienne, A.S., Maurer, R., Boulens, V., Levy, A., Rowe, T., 2004. Resetting the path integrator: a basic condition for route-based navigation. J. Exp. Biol. 207 (9), 1491–1508.
Gallistel, C.R., 1990. The Organization of Learning. The MIT Press, Cambridge, MA.
Gil, M., Ancau, M., Schlesiger, M.I., Neitz, A., Allen, K., De Marco, R.J., Monyer, H., 2018. Impaired path integration in mice with disrupted grid cell firing. Nat. Neurosci. 21 (1), 81–91.
Hafting, T., Fyhn, M., Molden, S., Moser, M.-B., Moser, E.I., 2005. Microstructure of a spatial map in the entorhinal cortex. Nature 436 (7052), 801–806.
Hargreaves, E.L., Rao, G., Lee, I., Knierim, J.J., 2005. Major dissociation between medial and lateral entorhinal input to dorsal hippocampus. Science 308 (5729), 1792–1794.
Howard, L.R., Javadi, A.H., Yu, Y., Mill, R.D., Morrison, L.C., Knight, R., et al., 2014. The hippocampus and entorhinal cortex encode the path and Euclidean distances to goals during navigation. Curr. Biol. 24 (12), 1331–1340.
Høydal, Ø.A., Skytøen, E.R., Andersson, S.O., Moser, M.-B., Moser, E.I., 2019. Object-vector coding in the medial entorhinal cortex. Nature 568 (7752), 400–404.
In, M.-H., Speck, O., 2012. Highly accelerated PSF-mapping for EPI distortion correction with improved fidelity. Magma Magn. Reson. Mater. Phys. Biol. Med. 25 (3), 183–192.
Jacob, P.-Y., Gordillo-Salas, M., Facchini, J., Poucet, B., Save, E., Sargolini, F., 2017. Medial entorhinal cortex and medial septum contribute to self-motion-based linear distance estimation. Brain Struct. Funct. 222 (6), 2727–2742.
Jeffreys, H., 1961. The Theory of Probability, third ed. Oxford University Press, Oxford, UK.
Kearns, M.J., Warren, W.H., Duchon, A.P., Tarr, M.J., 2002. Path integration from optic flow and body senses in a homing task. Perception 31 (3), 349–374.
Kelly, J.W., McNamara, T.P., Bodenheimer, B., Carr, T.H., Rieser, J.J., 2008. The shape of human navigation: how environmental geometry is used in maintenance of spatial orientation. Cognition 109 (2), 281–286.
Kentros, C.G., Agnihotri, N.T., Streater, S., Hawkins, R.D., Kandel, E.R., 2004. Increased attention to spatial context increases both place field stability and spatial memory. Neuron 42 (2), 283–295.
Klatzky, R.L., 1998. Allocentric and egocentric spatial representations: definitions, distinctions, and interconnections. In: Freksa, C., Habel, C., Wender, K.F. (Eds.), Spatial Cognition. Lecture Notes in Computer Science, vol.1404. Springer, Berlin, Heidelberg.
Knierim, J.J., Neunuebel, J.P., Deshmukh, S.S., 2014. Functional correlates of the lateral and medial entorhinal cortex: objects, path integration and local–global reference frames. Philos. Trans. R. Soc. B 369 (1635), 20130369.
Kropff, E., Carmichael, J.E., Moser, M.-B., Moser, E.I., 2015. Speed cells in the medial entorhinal cortex. Nature 523 (7561), 419–424.
Kunz, L., Schröder, T.N., Lee, H., Montag, C., Lachmann, B., Sariyska, R., et al., 2015. Reduced grid-cell–like representations in adults at genetic risk for Alzheimer's disease. Science 350 (6259), 430–433.
Kuruvilla, M.V., Ainge, J.A., 2017. Lateral entorhinal cortex lesions impair local spatial frameworks. Front. Syst. Neurosci. 11, 30.
Loomis, J.M., Klatzky, R.L., Golledge, R.G., Cicinelli, J.G., Pellegrino, J.W., Fry, P.A., 1993. Nonvisual navigation by blind and sighted: assessment of path integration ability. J. Exp. Psychol. Gen. 122 (1), 73–91.
Lu, L., Leutgeb, J.K., Tsao, A., Henriksen, E.J., Leutgeb, S., Barnes, C.A., et al., 2013. Impaired hippocampal rate coding after lesions of the lateral entorhinal cortex. Nat. Neurosci. 16 (8), 1085–1093.
Maass, A., Berron, D., Libby, L.A., Ranganath, C., Düzel, E., 2015. Functional subregions of the human entorhinal cortex. Elife 4, e06426.
Marlinsky, V., 1999. Vestibular and vestibulo-proprioceptive perception of motion in the horizontal plane in blindfolded man—I. Estimations of linear displacement. Neuroscience 90 (2), 389–394.
McNaughton, B.L., Battaglia, F.P., Jensen, O., Moser, E.I., Moser, M.-B., 2006. Path integration and the neural basis of the "cognitive map.". Nat. Rev. Neurosci. 7 (8), 663–678.
Mittelstaedt, M.-L., Mittelstaedt, H., 1980. Homing by path integration in a mammal. Naturwissenschaften 67 (11), 566–567.
Morgan, L.K., MacEvoy, S.P., Aguirre, G.K., Epstein, R.A., 2011. Distances between real-world locations are represented in the human hippocampus. J. Neurosci. 31 (4), 1238–1245.
Moser, E.I., Kropff, E., Moser, M.-B., 2008. Place cells, grid cells, and the brain's spatial representation system. Annu. Rev. Neurosci. 31, 69–89.
Moser, E.I., Moser, M.-B., 2008. A metric for space. Hippocampus 18 (12), 1142–1156.
Nardini, M., Jones, P., Bedford, R., Braddick, O., 2008. Development of cue integration in human navigation. Curr. Biol. 18 (9), 689–693.
Nathaniel Phillips, 2017. A Companion to the e-Book "YaRrr!: The Pirate's Guide to R" (Version R package version 0.1.5). Retrieved from. https://CRAN.R-project.org/package=yarrr.
Nichols, T.E., Holmes, A.P., 2002. Nonparametric permutation tests for functional neuroimaging: a primer with examples. Hum. Brain Mapp. 15 (1), 1–25.
Nielson, D.M., Smith, T.A., Sreekumar, V., Dennis, S., Sederberg, P.B., 2015. Human hippocampus represents space and time during retrieval of real-world memories. Proc. Natl. Acad. Sci. U.S.A. 112 (35), 11078–11083.
Parron, C., Poucet, B., Save, E., 2004. Entorhinal cortex lesions impair the use of distal but not proximal landmarks during place navigation in the rat. Behav. Brain Res. 154 (2), 345–352.
Parron, C., Save, E., 2004. Evidence for entorhinal and parietal cortices involvement in path integration in the rat. Exp. Brain Res. 159 (3), 349–359.
Pessoa, L., Gutierrez, E., Bandettini, P.A., Ungerleider, L.G., 2002. Neural correlates of visual working memory: fMRI amplitude predicts task performance. Neuron 35 (5), 975–987.
Philbeck, J.W., Behrmann, M., Levy, L., Potolicchio, S.J., Caputy, A.J., 2004. Path integration deficits during linear locomotion after human medial temporal lobectomy. J. Cogn. Neurosci. 16 (4), 510–520.
Reagh, Z.M., Yassa, M.A., 2014. Object and spatial mnemonic interference differentially engage lateral and medial entorhinal cortex in humans. Proc. Natl. Acad. Sci. U.S.A. 111 (40), E4264–E4273.
Rouder, J.N., Speckman, P.L., Sun, D., Morey, R.D., Iverson, G., 2009. Bayesian t tests for accepting and rejecting the null hypothesis. Psychon. Bull. Rev. 16 (2), 225–237.
Ruddle, R.A., Lessels, S., 2006. For efficient navigational search, humans require full physical movement, but not a rich visual scene. Psychol. Sci. 17 (6), 460–465.
Ruddle, R.A., Lessels, S., 2009. The benefits of using a walking interface to navigate virtual environments. ACM Trans. Comput. Hum. Interact. 16 (1), 1–18, 5.
Schindler, A., Bartels, A., 2013. Parietal cortex codes for egocentric space beyond the field of view. Curr. Biol. 23 (2), 177–182.
Schröder, T.N., Haak, K.V., Jimenez, N.I.Z., Beckmann, C.F., Doeller, C.F., 2015. Functional topography of the human entorhinal cortex. Elife 4, e06738.
Schultz, H., Sommer, T., Peters, J., 2012. Direct evidence for domain-sensitive functional subregions in human entorhinal cortex. J. Neurosci. 32 (14), 4716–4723.
Sherrill, K.R., Erdem, U.M., Ross, R.S., Brown, T.I., Hasselmo, M.E., Stern, C.E., 2013. Hippocampus and retrosplenial cortex combine path integration signals for successful navigation. J. Neurosci. 33 (49), 19304–19313.
Shettleworth, S.J., Sutton, J.E., 2005. Multiple systems for spatial learning: dead reckoning and beacon homing in rats. J. Exp. Psychol. Anim. Behav. Process. 31 (2), 125–141.
Shrager, Y., Kirwan, C.B., Squire, L.R., 2008. Neural basis of the cognitive map: path integration does not require hippocampus or entorhinal cortex. Proc. Natl. Acad. Sci. U.S.A. 105 (33), 12034–12038.
Stangl, M., Achtzehn, J., Huber, K., Dietrich, C., Tempelmann, C., Wolbers, T., 2018. Compromised grid-cell-like representations in old age as a key mechanism to explain age-related navigational deficits. Curr. Biol. 28 (7), 1–8.
Sutton, J.E., Joanisse, M.F., Newcombe, N.S., 2010. Spinning in the scanner: neural correlates of virtual reorientation. J. Exp. Psychol. Learn. Mem. Cogn. 36 (5), 1097–1107.
Tolman, E.C., 1948. Cognitive maps in rats and men. Psychol. Rev. 55 (4), 189–208.
Wang, C., Chen, X., Lee, H., Deshmukh, S.S., Yoganarasimha, D., Savelli, F., Knierim, J.J., 2018. Egocentric coding of external items in the lateral entorhinal cortex. Science 362 (6417), 945–949.
Wang, R.F., 2016. Building a cognitive map by assembling multiple path integration systems. Psychon. Bull. Rev. 23 (3), 692–702.
Wilson, D.I., Langston, R.F., Schlesiger, M.I., Wagner, M., Watanabe, S., Ainge, J.A., 2013. Lateral entorhinal cortex is critical for novel object-context recognition. Hippocampus 23 (5), 352–366.
Wilson, P.N., Alexander, T., 2008. Blocking of spatial learning between enclosure geometry and a local landmark. J. Exp. Psychol. Learn. Mem. Cogn. 34 (6), 1369–1376.
Witter, M.P., 1993. Organization of the entorhinal—hippocampal system: a review of current anatomical data. Hippocampus 3 (S1), 33–44.
Witter, M.P., Doan, T.P., Jacobsen, B., Nilssen, E.S., Ohara, S., 2017. Architecture of the entorhinal cortex: a review of entorhinal anatomy in rodents with some comparative notes. Front. Syst. Neurosci. 11, 46.
Wolbers, T., Hegarty, M., Buchel, C., Loomis, J.M., 2008. Spatial updating: how the brain keeps track of changing object locations during observer motion. Nat. Neurosci. 11 (10), 1223–1230.
Wolbers, T., Wiener, J.M., Mallot, H.A., Büchel, C., 2007. Differential recruitment of the hippocampus, medial prefrontal cortex, and the human motion complex during path integration in humans. J. Neurosci. 27 (35), 9408–9416.
Yoganarasimha, D., Rao, G., Knierim, J.J., 2011. Lateral entorhinal neurons are not spatially selective in cue-rich environments. Hippocampus 21 (12), 1363–1374.
Yushkevich, P.A., Piven, J., Hazlett, H.C., Smith, R.G., Ho, S., Gee, J.C., Gerig, G., 2006. User-guided 3D active contour segmentation of anatomical structures: significantly improved efficiency and reliability. Neuroimage 31 (3), 1116–1128.
Zhao, M., Warren, W.H., 2015. How you get there from here: interaction of visual landmarks and path integration in human navigation. Psychol. Sci. 26 (6), 915–924.